Urban Signatures in the Spatial Clustering of Precipitation Extremes over Mainland China

DASHAN WANG,[a,b] XIANWEI WANG,[a] LIN LIU,[c,d] DAGANG WANG,[a] AND ZHENZHONG ZENG[b]

[a] *School of Geography and Planning, Sun Yat-sen University, Guangzhou, China*
[b] *School of Environmental Science and Engineering, Southern University of Science and Technology, Shenzhen, China*
[c] *School of Geography and Remote Sensing, Guangzhou University, Guangzhou, China*
[d] *Department of Geography, University of Cincinnati, Cincinnati, Ohio*

(Manuscript received 2 March 2020, in final form 16 December 2020)

ABSTRACT: Urban areas demonstrate great influence on precipitation, yet the spatial clustering features of precipitation are still unclear over urban areas. This study quantitatively examines the spatial clustering of precipitation intensity in 130 urban-affected regions over mainland China during 2008–15 using a high-resolution merged precipitation product. Results show that the spatial heterogeneity patterns display diverse distribution and vary with precipitation intensity and urban sizes. Extreme and heavy precipitation has higher spatial heterogeneity than light precipitation over the urban-affected regions of grade 1 cities, and their mean Moran's I are 0.49, 0.47, and 0.37 for the intensity percentiles of ≥95%, 75%–95%, and <75%, respectively. The urban signatures in the spatial clustering of precipitation extremes are observed in 37 cities (28%), mainly occurring in the Haihe River basin, the Yangtze River basin, and the Pearl River basin. The spatial clustering patterns of precipitation extremes are affected by the local dominant synoptic conditions, such as the heavy storms of convective precipitation in Beijing (Moran's $I = 0.47$) and the cold frontal system in the Pearl River delta (Moran's $I = 0.78$), resulting in large regional variability. The role of urban environments for the spatial clustering is more evident in wetter conditions [e.g., relative humidity (RH) > 75% over Beijing and RH > 85% over the Pearl River delta] and warmer conditions ($T > 25$°C over Beijing and $T > 28$°C over the Pearl River delta). This study highlights the urban modification on the spatial clustering of some precipitation extremes, and calls for precautions and adaptation strategies to mitigate the adverse effect of the highly clustered extreme rainfall events.

KEYWORDS: Atmosphere-land interaction; Precipitation; Classification; Urban meteorology

1. Introduction

Heavy precipitation often demonstrates considerably uneven spatiotemporal characteristics (Dai et al. 2007). The spatial variance and the intensification of precipitation extremes have drawn increasing attention due to their crucial impacts on society and human life (Trenberth et al. 2003; Ghosh et al. 2012). The highly spatial clustered precipitation events could exert devastating effects on local areas. For example, an extreme rainfall occurred in Beijing on 21 July 2012 and brought more than 100 mm of precipitation to nearly 90% of the urban area and 460 mm to the storm center in the Fangshan district, resulting in severe life and economic loss (Zhang et al. 2013). Advances in the understanding of the precipitation heterogeneity not only allow for a comprehensive view of the storm system but also for the flood response and the adaptation management of hydrological hazards (Sun et al. 2017; Renard 2017).

The spatial heterogeneity of precipitation is evident at a regional scale. Precipitation variability induced by large-scale forcing (e.g., monsoon system, typhoon, and El Niño–Southern Oscillation) has been documented by numerous studies (Prat and Nelson 2013; Deng et al. 2014). In contrast, the spatial heterogeneity features of precipitation at the local scale are less clear (Zhou et al. 2019). Local surface conditions such as land cover, vegetation, soil texture, and topography play profound roles on the fluxes of heat, water vapor, momentum, carbon dioxide, and aerosol, and thus affect the spatial heterogeneity of precipitation (Feddema et al. 2005; Pielke et al. 2011). Especially urban areas have substantial contrasts in temperature, wind speed, and humidity against their rural surroundings, producing peculiar atmospheric circulations, and spatial variation of precipitation at a local scale. The urban heat island (UHI) effect, large land surface roughness, and high aerosol concentrations are considered as the main factors affecting precipitation extremes in urban environments (Han et al. 2014).

There is an ongoing debate on the impact of urban environment on precipitation variations at a local scale. Most observational and modeling research showed that urban environments play a positive role in affecting precipitation variety by enhancing moisture convergence, destabilizing the planetary boundary layer, and favoring vertical updrafts (Huff and Changnon 1973; Mote et al. 2007; Shepherd et al. 2010; Wang et al. 2015). Warmer temperatures and the reshaped surface energy partitioning may eventually form the UHI circulation, which could promote water vapor convergence and upward transport over urbanized areas, thus triggering local convective systems. However, several studies have found opposite effects that urban surface causes inhibition of convective available potential energy (CAPE) and reduction of local

Supplemental information related to this paper is available at the Journals Online website: https://doi.org/10.1175/JHM-D-20-0063.s1.

Corresponding author: Xianwei Wang, wangxw8@mail.sysu.edu.cn

DOI: 10.1175/JHM-D-20-0063.1

precipitation through absorbing more solar radiation, decreasing evapotranspiration, and surface moisture (Kaufmann et al. 2007; Zhang et al. 2009; Georgescu et al. 2012). In addition, urban aerosols may enhance or inhibit precipitation depending on the cloud and environmental conditions and aerosol concentration levels (Rosenfeld et al. 2008). Meanwhile, urban environments can play different but significant roles in precipitation distribution under various synoptic conditions. For instance, urban areas can initiate local convective activities and modify the intensity and structure of passing storms (Niyogi et al. 2011; Ashley et al. 2012), reshape and enhance frontal-type precipitation (Yu and Liu 2015), and increase the precipitation intensity during monsoon season (Shastri et al. 2015). The impact magnitude is closely associated with the size of urban areas (Miao et al. 2011; Schmid and Niyogi 2013). Nevertheless, our understandings of urban impacts on precipitation heterogeneity under different synoptic forcings are still far from clarity (Yang et al. 2019).

Most urban areas have been dramatically extended during the past 40 years in mainland China (Bloom 2011). At the same time, precipitation characteristics have experienced significant changes as well (Zhai et al. 2005; Sun et al. 2017). Particularly, the difference in precipitation intensity between urban areas and their surrounding regions has been magnified with the expansion of urbanization (Ren 2015). Although the urban effect on precipitation remains a puzzling issue, it is convincing that the urban signatures, which mean the urban modification of precipitation patterns and extremes through dynamic and thermodynamic effects of the urban environment (Li et al. 2011; Yang et al. 2014), could be detected in some typical cities (Yu and Liu 2015; Zhong et al. 2017; Wang et al. 2018). Highly clustered precipitation can result in severe hydrological impacts such as flash floods and waterlogging in urban areas, calling for the need of systematic examination of spatial heterogeneity of precipitation over urban-affected regions in China. As urban areas continue to extend, the risks of extreme events and rainfall variability may increase. However, analyses of the spatial clustering features of precipitation over urban areas are limited mainly due to the coarse resolution of observations. Accurate measurement of precipitation at the finer spatiotemporal scale could better represent the characteristics of precipitation in local areas (Chen et al. 2016). Moreover, most studies focus on typical rainfall events and in a few metropolitan areas (e.g., Beijing, Shanghai, and Guangzhou) over China (Wang et al. 2012). The urban effect on precipitation heterogeneity and clustering for other cities was not clear, which limits the transferability of their findings (Yang et al. 2014).

This study aims to provide a holistic investigation of the urban signatures in the spatial clustering of precipitation extremes and the underlying mechanisms at an urban scale in the present-day climate. More precisely, the objectives of this study are to 1) investigate the spatial heterogeneity features of precipitation at urban scale using a merged high-resolution precipitation dataset over mainland China and 2) identify the urban signatures in the spatial clustering of local precipitation extremes under different synoptic conditions and reveal the favorable backgrounds for urban effects.

2. Materials and methods

a. Data

The hourly China Merged Precipitation Analysis (CMPA) product was used in this study to explore the spatial heterogeneity of precipitation from 2008 to 2015 (Fig. 1a). The CMPA was derived from merging dense rain gauge network observations (~30 000 automatic weather stations) from the China Meteorology Administration (CMA) with the Climate Prediction Center morphing technique (CMORPH) satellite-based quantitative precipitation estimates (Joyce et al. 2004). It is in 0.1°/hourly resolution and starts from January 2008 to present over mainland China (Shen et al. 2014). This product shows good performance over urban areas due to the adjustment from dense rain gauges (Chen et al. 2016; Wang et al. 2019).

A percentile index was defined using the hourly CMPA data in order to detect the spatial heterogeneity of precipitation. For each grid across mainland China, all wet hours ($\geq$0.1 mm h^{-1}) were divided into three categories: light (<75th percentile), heavy (75th–95th percentile), and extreme ($\geq$95th percentile). Their mean precipitation intensities were marked as RI0, RI75, and RI95, respectively. The percentile-based index is more suitable and less affected by the scale mismatch for the spatial comparison of precipitation intensities in different urban areas (Zhang et al. 2011). In addition, we analyzed the frequency of extreme rainfall events, defined as the number of hours when the hourly rainfall is no less than 16 mm, and provided a statistic comparison in terms of ''hour-count'' information in regional analysis. The threshold of hourly extreme rainfall was adopted following the practice of the CMA.

The Japanese 55-year Reanalysis (JRA-55) data (Kobayashi et al. 2015) on 6-hourly and approximately 0.56° resolution from 2008 to 2015 were used to derive the clusters of synoptic conditions over the two selected metropolitan areas of the Beijing and Pearl River delta (see section 2d for detail). The JRA-55 data show better performance compared to other reanalysis products over mainland China (Chen et al. 2014). The CMA Land Data Assimilation System (CLDAS) v2.0 on 0.0625°/hourly resolution during 2008–15 was used to reveal the favorable backgrounds for urban effects under different synoptic clusters (Shi et al. 2011). We obtained surface pressure, air temperature at 2 m, and specific humidity at 2 m from the CLDAS data, and calculated the relative humidity (RH) within a grid using Eq. (1):

$$\mathrm{RH} = \frac{e}{e_{\mathrm{sat}}} \times 100\% = \frac{q \times P/0.622/1000}{0.6108 \times \exp\left(\dfrac{17.27 \times T}{237.3 + T}\right)} \times 100\%, \tag{1}$$

where q is specific humidity (g g^{-1}), P is the surface pressure (Pa), and T is the air temperature (°C). To match the precipitation data grid, both air temperature and RH were averaged to a daily scale and then resampled into the 0.1° × 0.1° grid using the bilinear interpolation method.

The land use/land cover dataset, the extent of main basins, the administrative boundary, and the center of prefecture-level cities in mainland China were provided by the Resource and Environment Data Cloud Platform of the Chinese Academy of

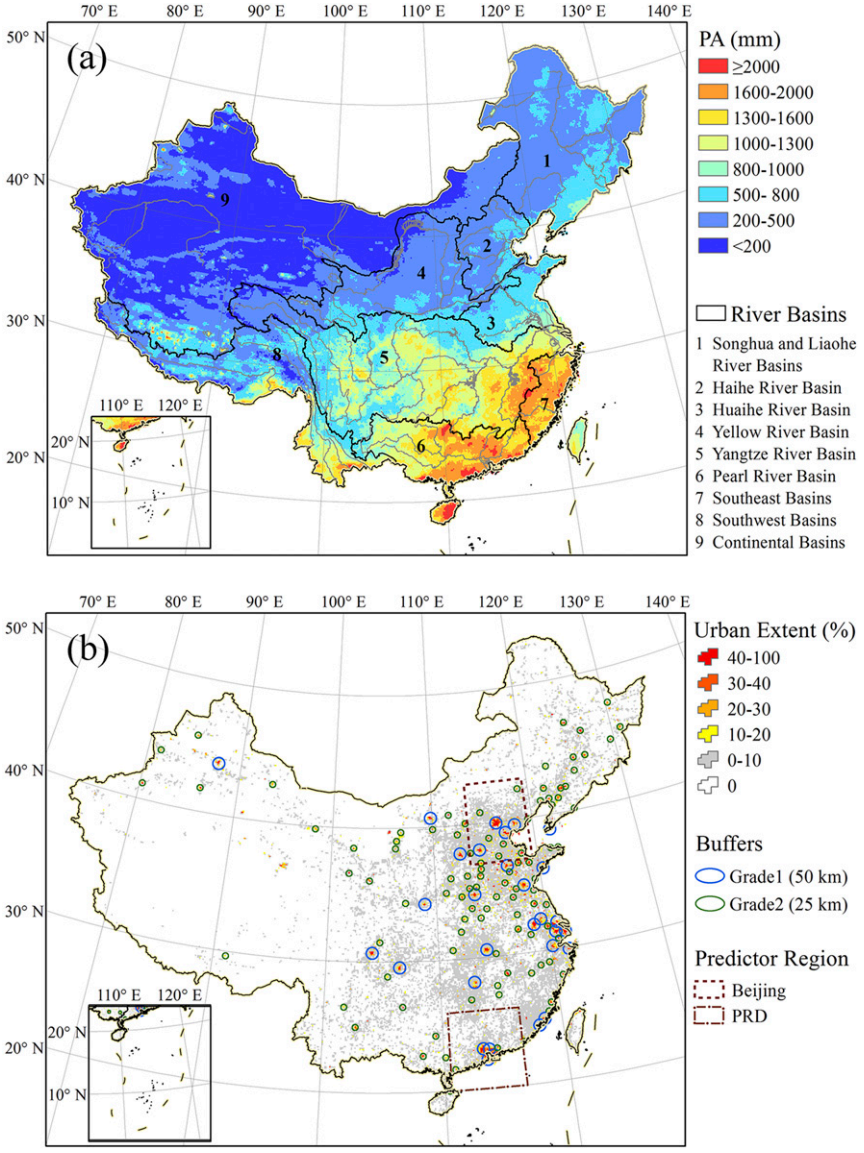

FIG. 1. (a) The annual mean precipitation (PA; mm) over mainland China derived from the CMPA product during 2008–15 and the nine main river basins. (b) The spatial distribution of urban extent and the locations of 130 urban-affected regions with a 50-km buffer (for grade 1 cities) and a 25-km buffer (for grade 2 cities). The 6° × 6° regions of Beijing (39°–41°N, 115.5°–117.5°E) and the PRD (22°–24°N, 112.5°–114.5°E) are outlined.

Sciences. The urban areas in mainland China were obtained using the land use/land cover data in 2010 (Liu et al. 2005), which were derived from Landsat TM/ETM+ (Thematic Mapper and Enhanced Thematic Mapper Plus) and *CBERS-1* (China–Brazil Earth Resources Satellite) images. It provides dominant land cover classifications (farmland, forest, grassland, water body, or urban) at 100-m pixels.

b. Urban-affected regions

We investigated the spatial heterogeneity features of precipitation at urban-affected regions (UARs). The overall framework for defining UARs and spatial heterogeneity patterns is provided in Fig. 2a. The land cover data were reclassified into two classes, urban and nonurban. The percentage of urban extent was calculated by dividing the number of 100-m urban pixels with the total number of pixels within each 0.1° × 0.1° grid (Fig. 1b). Schmid and Niyogi (2013) have demonstrated that a radius of 20 km is the threshold of city size to modify thunderstorms. Therefore, we tested different percentage thresholds of the urban fraction to determine urban grids by calculating the total number of urban grids over 333 prefecture-level cities in mainland China and the number of cities with four urban grids or more (the minimum requirement for a radius of 20 km). As the threshold increases from 1% to

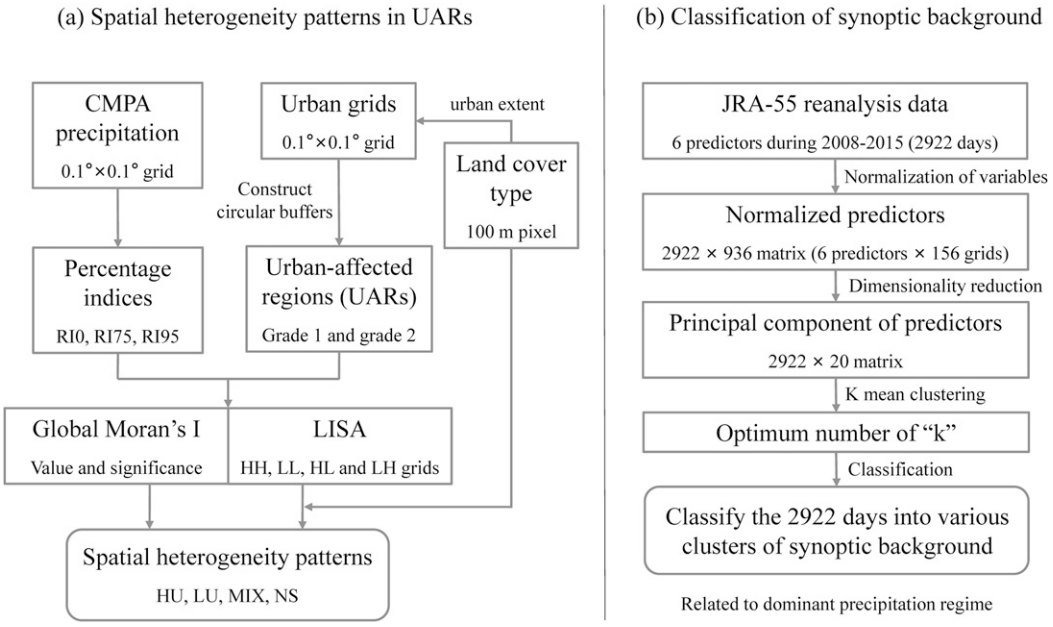

FIG. 2. Overview of section 2: (a) framework for defining urban-affected regions and the spatial heterogeneity patterns and (b) flowchart of the synoptic background classification.

10%, the number of urban grids (cities) rapidly reduces from 2998 grids (290 cities) to 1288 grids (125 cities). When the threshold increases to 50%, urban grids (cities) reduce to 202 grids (25 cities) (Fig. 3a). Considering the extent of urban effect on precipitation and the coverage of study cities, we choose the 10% threshold to define the 0.1° × 0.1° urban grids.

The UARs were defined using the 0.1° × 0.1° urban grids by three steps. First, the number of spatial consecutive urban grids was calculated within each prefecture-level city's administrative boundary. Then all cities were divided into two grades: grade 1 cities with 16 urban grids or more (ensure a radius larger than 20 km), and grade 2 cities with urban grids greater or equal to 4 but less than 16. Exceptionally, five provincial capitals with three urban grids were also included in grade 2 cities. Next, the UARs were determined by constructing uniform circular buffers around the urban center as the spatial heterogeneity index is dependent on the extent of analysis area. Previous studies employed different buffers to generate urban influence regions, such as 100-km buffers in Shastri et al. (2015) and 25-km buffers used by Luo and Lau (2018). We tested three circular buffers with a radius of 25, 50 and 100 km. The proportion of urban grids in the three buffers (or UARs) are 64.7%, 36.4% and 22.7% for grade 1 cities and 26.9%, 12.4% and 8.9% for grade 2 cities (Fig. 3b). To better compare

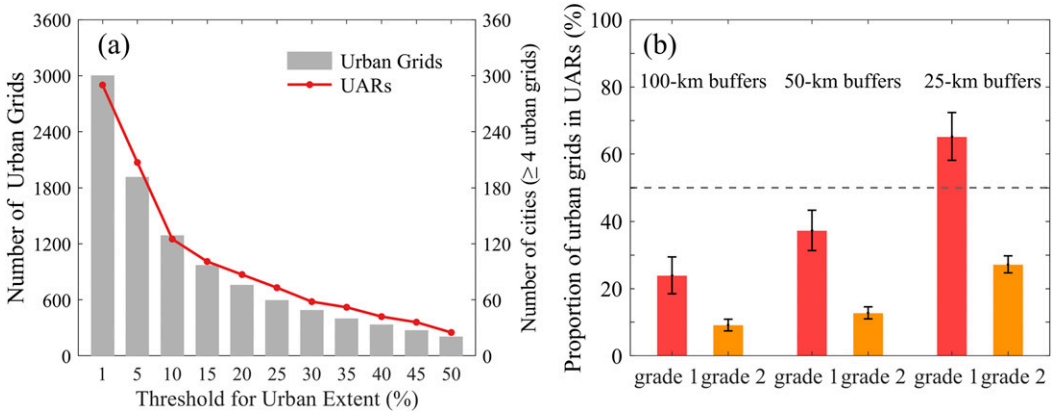

FIG. 3. (a) Estimation of the number of urban grids (bars; left *y* axis) and the number of cities with four urban grids or more (line; right *y* axis) using different thresholds of urban extent for defining urban grids. (b) The proportion of urban grids to the total grids over the two-grade UARs using three sizes of buffer radius. Error bars show the 95% confidence intervals of the proportion.

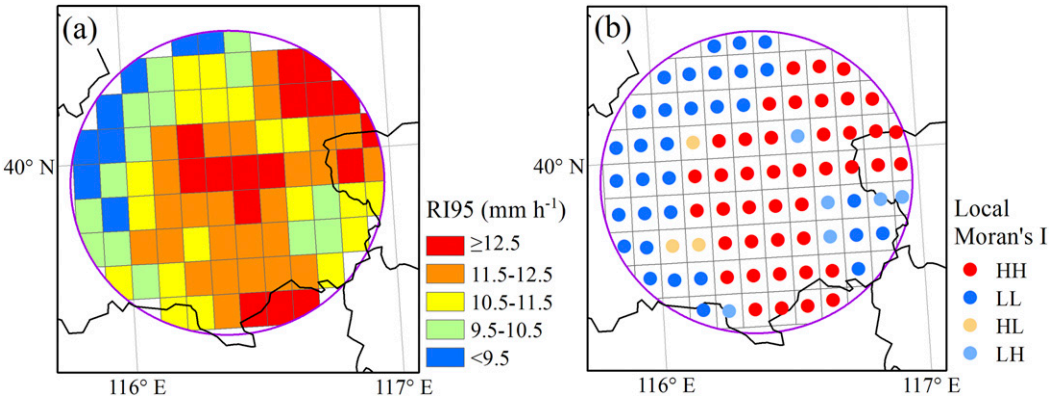

FIG. 4. The spatial distribution of (a) hourly precipitation of RI95 (global Moran's $I = 0.65$; $Z > 1.96$) and (b) the spatial heterogeneity pattern determined by local Moran's I (HU) in the urban-affected region of Beijing.

the spatial heterogeneity under similar proportion of urban grids and nonurban grids, the UARs were constructed by the 50- and 25-km buffers around the urban center for cities in grade 1 and grade 2, respectively. Those grade 2 cities that are enclosed by the 50-km circular buffers of neighboring grade 1 cities were excluded in the further analysis (e.g., Fig. S1 in the online supplemental material). Finally, total 30 UARs in grade 1 and 100 UARs in grade 2 were identified in mainland China (Fig. 1b).

We further analyzed the regional variations for the spatial heterogeneity patterns of precipitation intensity at UARs over the nine main river basins in mainland China (Fig. 1a), to minimize the difference of the topography, climate pattern, and precipitation characteristics in each subregion (Miao et al. 2016).

c. *Spatial heterogeneity pattern*

The Moran's I index, which is a common method to character spatial autocorrelation and reveal the structure of regional variables (Renard 2017), was adopted to quantitatively investigate the spatial heterogeneity of precipitation in UARs. First, the global Moran's I (Moran 1950) value was employed to quantify the level of spatial heterogeneity for precipitation indices in each UAR, and was calculated in Eq. (2):

$$I = \frac{n}{\sum_{i=1}^{n}\sum_{j=1}^{n} W_{ij}} \frac{\sum_{i=1}^{n}\sum_{j=1}^{n} W_{ij}(R_i - \overline{R})(R_j - \overline{R})}{\sum_{i=1}^{n}(R_i - \overline{R})^2}, \tag{2}$$

where n is the number of grids indexed by i and j; R_i and R_j are the variables for grid i and j, respectively; $\overline{R}$ is the spatial average of variables; and W_{ij} is the spatial weight between grid i and j (1 or 0) according to their spatial adjacency. The global Moran's I value compares the difference between each pair of neighbors to the mean difference between all features in the study area, i.e., two categories of UARs defined in this study. It varies between -1 and 1. A Z score larger than 1.96 or less than -1.96 indicates that the spatial heterogeneity was statistically significant at the 95% confidence level. If the average difference between neighboring features was less (more) than that among all features, the Moran's I value would be positive (negative) and indicated a spatial clustered (dispersed) pattern. The global Moran's I value close to 0 and an absolute value of Z score no larger than 1.96 indicated a random distribution.

The local Moran's I referred to as the local indicators of spatial association (LISA; Anselin 1995) was applied to identify the key clusters of precipitation intensity in this study. The HH (LL) described a high (low) value cluster where nearby grids have similarly high (low) values, and was computed as the difference with its neighboring grids was smaller than that with all grids. The HL (LH) aberrant point represented a high (low) value surrounded by low (high) neighboring values and was defined as the difference with its neighboring grids was larger than that with all grids. Figure 4 illustrates an example for the spatial distribution of RI95, as well as the corresponding HH (LL) clusters and the aberrant points (HL and LH) over the UAR of Beijing.

Finally, the spatial distribution of precipitation features within each UARs were defined as one of the following four spatial heterogeneity patterns: HU, LU, MIX, and NS (Fig. 2a). These four patterns were distinguished based on the value and significance of the global Moran's I and the mean urban extent over HH and LL grids. If the Moran's I was significantly positive (Moran's $I > 0$, $Z > 1.96$; spatial clustered), then the mean urban extent over the HH grids, LL grids, and the whole UAR was computed (marked as U_H, U_L, and U_R, respectively). UARs with $U_H > U_R > U_L$ ($U_H < U_R < U_L$) relationship represented that HH (LL) grids were clustered in urban areas and was categorized as HU (LU); others, i.e., both U_H and U_L are higher (or lower) than U_R, were defined as MIX, which demonstrated that precipitation in this region was unevenly distributed but the urban signature was not evident. Whereas when the Moran's I was not significant ($|Z| \leq 1.96$), which indicated a random spatial distribution, this UAR was categorized as NS. The HU demonstrated the urban signatures in the spatial clustering of precipitation intensity (e.g., RI95 clustered over urban areas in the Beijing UAR; Fig. 4) and was the primary target analyzed in this study.

d. *Classification of synoptic background*

To analyze and understand the urban signatures in precipitation extremes under different synoptic conditions, here we

take two specific areas of Beijing in the Haihe River basin and the Pearl River delta (PRD) in the Pearl River basin for further study. Beijing is one of the largest megacities in the world, and the PRD is known as the largest metropolitan agglomerations and densely populated areas. The urban signatures on the spatial clustering of precipitation are prominent in both areas. Details are presented in the section 3a. The Beijing metropolitan areas consist of mountainous areas in the northern and western parts and plain in the southern and eastern parts. The PRD is seated in the southern coast of China and contains the main cities of Guangzhou, Foshan, Dongguan, Shenzhen, and Zhongshan. Over the past decades, both Beijing and PRD have undergone rapid urban expansion and experienced extreme precipitation events and severe urban floods. Two $6^\circ \times 6^\circ$ regions which centers on the metropolitan areas of Beijing and PRD were defined as the predictor regions (Fig. 1b).

Considering the impacts of large-scale synoptic conditions on precipitation, the method of Shastri et al. (2015) was adopted to classify the study periods (days) into various clusters that represent different regional synoptic backgrounds (Fig. 2b). Six key meteorological variables were used to describe synoptic backgrounds, namely, air temperature, atmospheric pressure, relative humidity, vertical velocity, as well as the 500-hPa *U*-wind field and *V*-wind field derived from the JRA-55 reanalysis. Instead of using the raw 6-h data, the daily mean values of the six variables were used in order to mitigate the effect of diurnal variation. The processing involves three steps, normalization of variables, dimensionality reduction, and classification of synoptic backgrounds. We use Beijing as an example to illustrate the process. The predictor region consists of 156 (13×12) JRA-55 grids. First, each of the six meteorological predictors was normalized with the standardization method (Shastri et al. 2017) to eliminate the scale mismatch. Six normalized variables at 156 grids made a sum of 936 (6×156) dimensions as predictors, which form a 2922×936 matrix with their 2922 daily values during 2008–15. Using all dimensions of the predictors to classify the clusters would pose difficulty of multidimensionality and multicollinearity, so the second step was to apply the principal component analysis (PCA) technique to reduce the high dimensions. The reduced 20 (18) principal components for Beijing (PRD) could represent more than 95% of the variability of high-dimensioned predictors. Next, the unsupervised classification method of *k*-means clustering was carried out to partition the principal component vectors (e.g., the 2922×20 matrix for Beijing) into *k* clusters. This method was executed 20 times for each *k* value from 2 to 8 for the predictor region. The optimum numbers of *k* values were then identified as 5 and 6 corresponding to the highest value of Dunn's index for Beijing and PRD, respectively. Finally, we classified each day during the study period into one of the 5 (6) clusters for Beijing (PRD) based on the mode of cluster type in that day among the 20 times execution of the optimum *k* value.

All clusters and their mean conditions of the synoptic background in each cluster type of Beijing and PRD are presented in Figs. S2 and S3. Each cluster represents one type of synoptic condition, which is closely related to one dominant precipitation regime. For example, in the PRD (Fig. S3), precipitation in cluster 3 mainly occurs from mid-March to early May and is associated with the cold frontal system. Cluster 4 spans from mid-May to June when the southwestern monsoon dominates. Cluster 5 is coincident with tropical convective processes, with the observed high temperature and weak synoptic background. Cluster 6 represents the anticlockwise southeasterly wind of tropical cyclone events. Distinct differences could be observed between these types for the six variables, showing the ability of this approach in classifying and understanding the regional synoptic backgrounds (Singh et al. 2016; Gu et al. 2019). As the synoptic background remains fixed in each cluster type, the difference of precipitation heterogeneity features between the metropolitan areas could be attributed to the urban effects and other local factors (Shastri et al. 2015). In other words, the urban signature in the spatial clustering of precipitation extremes could be illustrated by such a difference.

3. Results and discussions

a. Regional variations for the spatial heterogeneity patterns of precipitation

1) Spatial heterogeneity features of precipitation

Precipitation intensity displays evident geographical heterogeneity across mainland China (Figs. 5a–c). Eastern and southern China generally have larger precipitation intensity in the three percentiles. For example, it increases from less than $5\ \mathrm{mm\ h^{-1}}$ in the western inland to more than $20\ \mathrm{mm\ h^{-1}}$ in the eastern coast for the RI95 (Fig. 5c). The precipitation intensity in southern China and Bohai Rim areas is much higher than in other regions. Some locations in the inland areas showed much larger intensities than their neighboring areas primarily due to the orographic effect or lake/reservoir effect. The abnormal high values over the Tibetan Plateau are likely due to the systematic anomalies of passive microwave (PMW) estimates over inland water bodies (Tang et al. 2016).

The spatial heterogeneity patterns (HU, LU, MIX, and NS; Fig. 2a) of precipitation intensity at the urban scale present diverse distribution (Figs. 5d–f). The HU represents the urban signature in promoting the clustering of precipitation intensity and is dominant across mainland China except for cities on the east coast, in the Huaihe River basin and in the inland areas of northwest China and the Tibetan Plateau. The HU takes up 40%, 34%, and 43% among the four patterns for the three percentiles of RI0, RI75, and RI95 in the grade 1 cities, being 35%, 38%, and 24% in the grade 2 cities, respectively (Figs. 5g,h). The LU represents that the high values of precipitation intensity are clustered in rural areas and is the second dominant pattern for grade 1 cities, accounting for 30%, 33%, and 30% for RI0, RI75, and RI95, but occupies very low proportions of 15%, 9%, and 24% for grade 2 cities, respectively. The LU regions are mainly located in the eastern coastal cities, where the monsoon or plum rainfall controls the annual precipitation (Figs. 5d–f). The MIX represents those cases that urban signatures in the spatial clustering of precipitation intensity are not prominent, and they mainly occur in the grade 1 cities with a proportion around 30% (Fig. 5g). The NS means

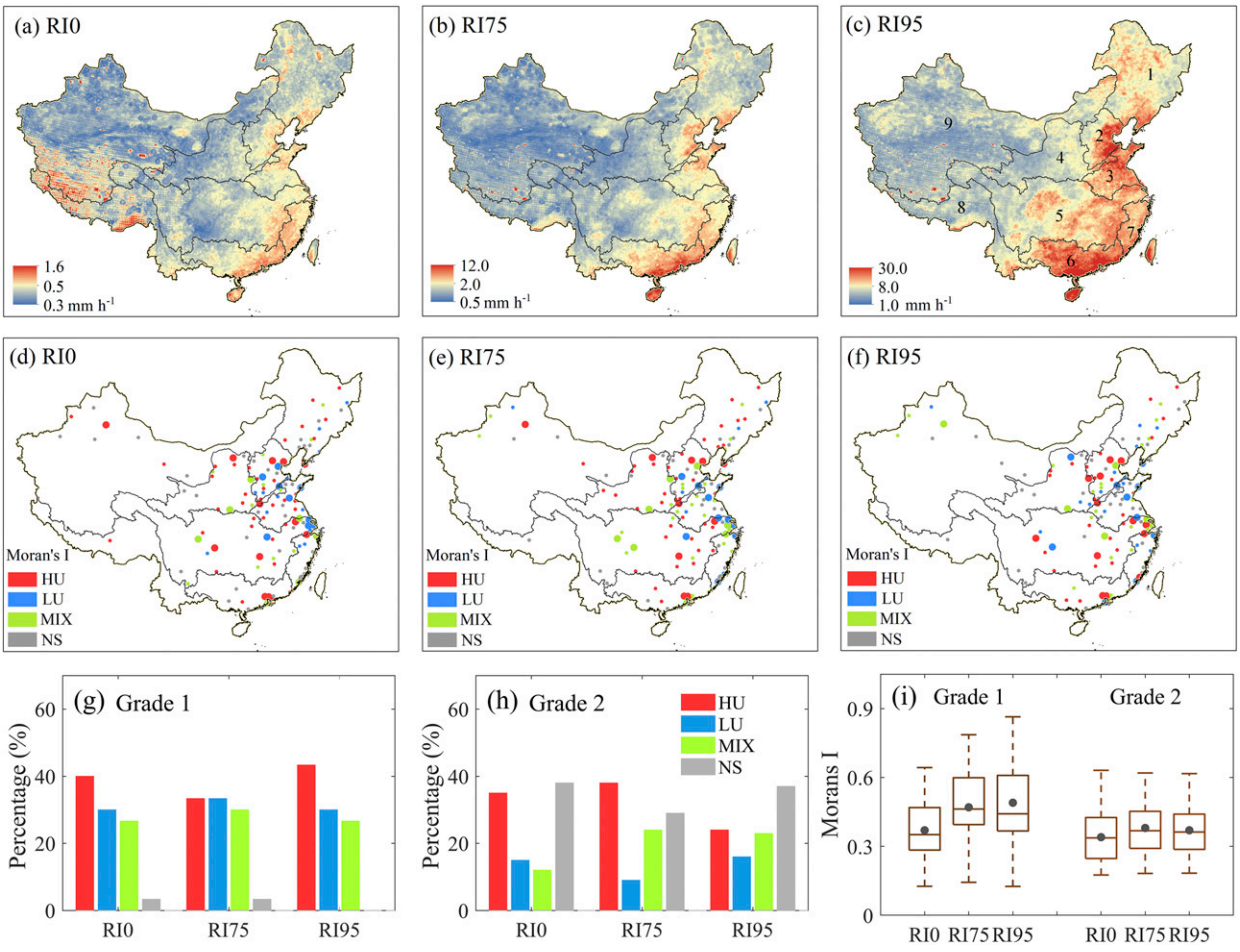

FIG. 5. The spatial distributions of (a)–(c) mean hourly precipitation (mm h^{-1}) and (d)–(f) four heterogeneity patterns (HU, LU, MIX, NS) for the three percentiles (RI0: 0–75th, RI75: 75–95th, RI95: 95–100th) from 2008 to 2015 over mainland China, (g),(h) the proportions of urban-affected regions for the four spatial heterogeneity patterns, and (i) the boxplots of the Moran's *I* value. The box represents the first and third quartiles, the line (dot) within the box represents the median (mean) value, and the whiskers represent 1.5 times the interquartile.

that precipitation intensity is in a random spatial distribution within the UAR, and primarily takes place in the grade 2 cities (accounts for 29%–38%; Fig. 5h). These indicate that the impact of the urban extent on the clustering of precipitation is associated with urban sizes. The metropolitan areas in the grade 1 cities have a larger impact on the clustering of precipitation extremes than the smaller urban areas in grade 2 cities, where there are higher NS proportions for precipitation intensity.

Figure 5i provides the statistic values of the Moran's *I* for the two sizes of urban areas. The values of Moran's *I* are larger in the grade 1 cities (with mean values of 0.37, 0.47 and 0.49 for the three percentiles, respectively) than those in the grade 2 cities (0.34, 0.38, and 0.37), and for heavy and extreme precipitation. This suggests that heavy and extreme precipitation tends to have more significant spatial clustering, especially over large urban areas.

The spatial heterogeneity of the frequency for light (<4 mm h^{-1}), heavy (4–16 mm h^{-1}), and extreme (≥16 mm h^{-1}) precipitation at urban scale were also analyzed (Fig. 6). In contrast to precipitation intensity, the frequency of light precipitation shows higher spatial heterogeneity (with mean Moran's *I* values of 0.56 and 0.38 for the two grades, respectively) than that of extreme precipitation (0.41 and 0.32) over UARs. LU is the dominant pattern for light precipitation (accounts for 47% in grade 1 cities and 36% in grade 2 cities), showing the signature of urban extents to the inhibition of precipitation frequency. The urban surface could disturb the radiation budget in the urban canopy, resulting in the pronounced reduction in latent heat flux, RH and evapotranspiration, and increases in sensible heat flux against their surroundings (Zhang et al. 2014). These processes could lead to negative effects on the initiation and development of precipitation systems. The fewer rain hours over urban areas could be partially explained by the above processes. MIX and NS show a higher proportion (added up to 53%–64%) in the grade 2 cities. HU is only prominent for the extreme precipitation frequency among grade 1 cities that are mainly located in the Haihe basin and

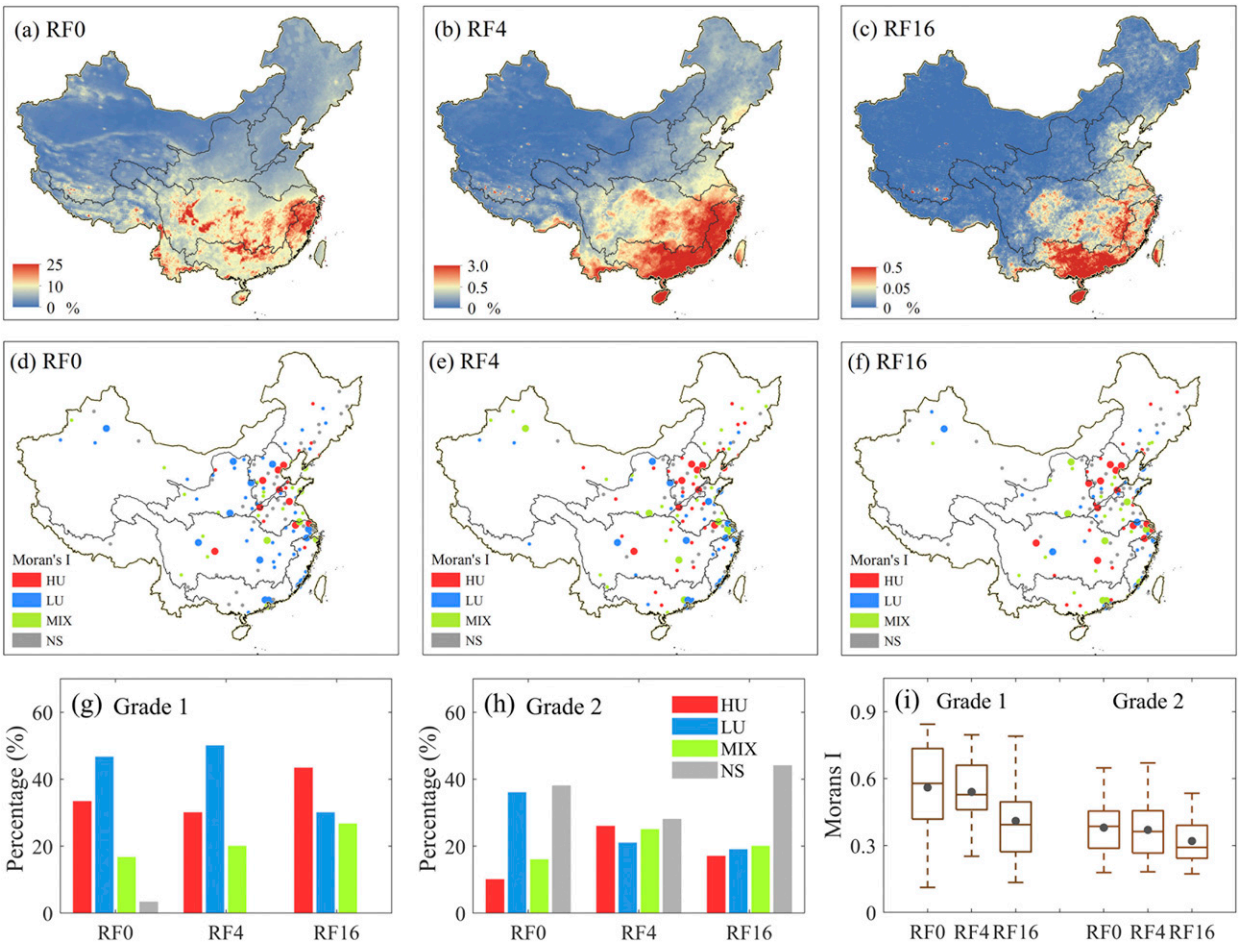

FIG. 6. The spatial distributions of (a)–(c) frequency (%) and (d)–(f) four heterogeneity patterns (HU, LU, MIX, NS) for the three indices (RF0: 0.1–4 mm h^{-1}, RF4: 4–16 mm h^{-1}, RF16: ≥16 mm h^{-1}) from 2008 to 2015 over mainland China; the frequency indices are computed as the ratio of the number of hours in the three thresholds to the total hours during the study period. (g),(h) The proportions of urban-affected regions for the four spatial heterogeneity patterns, and (i) the boxplots of the Moran's *I* value. The box represents the first and third quartiles, the line (dot) within the box represents the median (mean) value, and the whiskers represent 1.5 times the interquartile.

Yangtze River basin (Fig. 6f). In summary, urban signatures are more evident in the inhibition of light precipitation frequency and the spatial clustering of extreme precipitation intensity.

2) REGIONAL VARIATIONS

The urban extent may not be the dominant factor in the spatial heterogeneity of precipitation over the UARs in mainland China, but it is explicit from the results that the spatial clustering of precipitation varies distinctly in different regions, especially for precipitation extremes. For the extreme precipitation (RI95), HU and NS patterns share larger proportions (both are 28%) than the others (19% for LU and 24% for MIX) in the 130 UARs (Table 1). The HU pattern is dominant in the Yangtze River basin (48%), the Haihe River basin (44%), and the Pearl River basin (36%), which indicates that the local influence of urbanization mainly aggregates the spatial clustering of precipitation extremes. The LU and NS dominate in southeast China (56% and 33%), the Huaihe River basin (32% and 42%) and the Yellow River basin (28% and 33%), while NS occupies 100% in the southwest basin and 50% in the continental basins, suggesting that the local environmental setting and synoptic conditions determine the spatial clustering of precipitation extremes and the effect of urbanization on spatial clustering is negligible or even disperse the precipitation extremes. The MIX pattern is dominant (32%) in Songhua and Liaohe River basins, where each pattern shares a similar proportion.

In summary, precipitation heterogeneity at an urban scale is closely linked to climate features, topography relief, coastal boundaries, and urban development (Zhou et al. 2019). The regional variation for the spatial heterogeneity patterns of precipitation may be largely determined by the local climate setting and topography. For instance, the urban signatures in the spatial clustering of extreme precipitation intensity are not prominent over the Huaihe River basin (3), southeast China (7),

TABLE 1. City count and proportions of each heterogeneity pattern (RI95) in the nine main river basins of mainland China. Proportions higher than the national mean value are highlighted with bold font.

	Total	HU	LU	MIX	NS
1. Songhua and Liaohe River basins	19	4 (21%)	4 (21%)	**6 (32%)**	5 (26%)
2. Haihe River basin	18	**8 (44%)**	2 (11%)	4 (22%)	4 (22%)
3. Huaihe River basin	19	2 (11%)	**6 (32%)**	3 (16%)	**8 (42%)**
4. Yellow River basin	18	5 (28%)	**5 (28%)**	2 (11%)	**6 (33%)**
5. Yangtze River basin	27	**13 (48%)**	1 (4%)	**9 (33%)**	4 (15%)
6. Pearl River basin	11	**4 (36%)**	1 (9%)	**4 (36%)**	2 (18%)
7. Southeast basins	9	1 (11%)	**5 (56%)**	0 (0%)	**3 (33%)**
8. Southwest basins	1	0 (0%)	0 (0%)	0 (0%)	**1 (100%)**
9. Continental basins	8	0 (0%)	1 (13%)	**3 (38%)**	**4 (50%)**
Total (national)	130	37 (28%)	25 (19%)	31 (24%)	37 (28%)

and the continental basins (9) (Table 1 and Fig. 5f), suggesting the impact from large-scale circulations (e.g., monsoon and tropical cyclones) on precipitation extremes is greater than the local influence in the areas of the inner continent, plain terrain or coastal regions (Fig. S4). The Yangtze River delta (YRD) area in the lower reaches of Yangtze River basin has a low and flat terrain in the city cores and downwind regions, and mountainous terrain (Dabie Mountains and Huangshan Mountains) distributes in the upwind direction (Fig. S4). The combination of large-scale forcing such as the plum rainfall, land–sea circulation and the regional topography are considered as the dominant factors affecting the precipitation clustering in this region (Fu et al. 2019). Although there are clustered patterns of precipitation extremes, the urban signatures are not evident in the YRD (Figs. 5d–f). In the following session, we present two typical regions of Beijing and PRD, where urban areas impress a significant signature on the spatial clustering of the precipitation extremes.

b. *Favorable synoptic conditions of urban signatures in the spatial clustering of precipitation extremes*

1) TWO FAVORABLE SYNOPTIC CONDITIONS FOR URBAN EFFECTS

Previous modeling studies demonstrated that the role of urban areas on the heterogeneity of precipitation varies with geographical regions and synoptic conditions, as we summarized in Table 2, showing the modulating role of synoptic backgrounds for the urban effects on individual precipitation event. Here we put forward a hypothesis that urban signatures in the spatial clustering of precipitation vary with different synoptic background and the related precipitation types. The two metropolitan areas of Beijing and the PRD are selected as the regional analysis to investigate the urban signatures in precipitation extremes under different synoptic conditions. The metropolitan area is defined as the continuous urban grids with a proportion of urban extent $> 10\%$ and the suburban areas are defined as the surrounding grids within a three-grid distance. Those suburban grids having an elevation of higher than 800-m elevation or crossing the coastline are excluded to avoid the effect of other local effects such as topography and land–sea interaction (Figs. 7a and 8a).

In the Beijing domain, the climate is influenced by the East Asia summer monsoon (EASM) and the Siberian Express, characterized as hot and wet summers spanning from June to August, and cold and dry winters (Fig. S2). The two centers of annual mean precipitation over the Beijing city are in the urban core and the climatic downwind region (Fig. 7c). The significant HH clusters of RI95 are situated in the urban core for convective precipitation (Fig. 7e), while the HH clusters are primarily located in the urban downwind and secondarily in the urban core for monsoon precipitation, which is generally consistent with the total precipitation (Fig. 7f). The magnitudes of the Moran's I of RI95 for convective precipitation are the largest (0.47), followed by monsoon precipitation (0.41), indicating that the spatial clustering pattern of precipitation extremes over Beijing may be largely affected by these two types (Table 3). Moreover, convective precipitation shows an evident contrast between urban and suburban, with 1.0 mm h^{-1} higher of mean RI95 (Fig. 7h) and 64% more of extreme rainy hours over urban areas (Fig. 7g). The high temperature over urbanized areas and the relatively weak synoptic background suggest a favorable condition for the UHI impacts and convective processes (Fig. S2). Monsoon precipitation controls the spatial pattern of annual precipitation and contributes 50.9% of the annual precipitation and more than 80% to the extreme precipitation with only 14.3% of total days (Fig. 7f and Table 3). The urban downwind had larger precipitation than the urban area, while the urban area had larger values than the upwind and the suburb (Fig. 7f and Table 3). The transitional topography and the moisture supply from the Miyun reservoir which is located near the northeast boundary of Beijing, may contribute to the initiation and intensification of storms over the windward slope region, thus increasing the Beijing downwind precipitation (Yang et al. 2014). The cold frontal system in spring and autumn brings about 36% of the total precipitation each year while only contributes about 10% to the extremes each year (Table 2).

In the PRD, precipitation is controlled by different synoptic conditions in each season, such as the first rainy season from April to June and the second rainy season from July to September (Fig. S3). The annual precipitation is greatest in the southwest hilly coast and the northeast uplift transition area (Fig. 8c). The humid cold frontal precipitation mainly occurs from mid-March to early May and is a unique type in south China. Extreme precipitation is spatially clustered over urban areas and the value of the Moran's I of RI95 for cold frontal precipitation is as high as 0.78 (Table 4). Urban areas have 16%

TABLE 2. Modeling studies over mainland China used to investigate the urban effects on the spatial clustering of precipitation events. The urban signatures in spatial clustering of precipitation extremes varies with synoptic conditions and rainfall types. Note that daily mean temperature data and relative humidity data of these precipitation cases are obtained from the SURF_CLI_CHN_MUL_DAY_V3.0 dataset, downloaded from the China Meteorological Data Sharing Service System (www.nmic.cn/data/). The locations and site numbers of national stations that are used for providing areal mean temperature and RH over the study areas in these references are illustrated in Fig. S5.

ID	Region	Study period	Temp	RH	Synoptic condition	Factors	Heterogeneity change	References
a	Beijing	27 Jun 2008	21.5°C	87.8%	Cold frontal system	Land cover change	Aggregation (modify the precipitation distribution and enhance the maximum intensity)	Zhong and Yang (2015)
b	Beijing	27 Jun 2008	21.5°C	87.8%	The same as above	Land cover change, aerosol emission	Inhibition (land cover change aggregates rainfall clustering, while the inhibition for aerosol dominants in this case)	Zhong et al. 2015
c	Guangzhou	7 May 2017	24.6°C	92.6%	Slowly evolving synoptic conditions with continuously transported moisture	Land cover change	Aggregation (but in a lesser extent than synoptic and topographic effect)	Huang et al. (2019)
d	Yangtze River delta	10 Jun 2017	24.2°C	92.2%	Convective process affected by southwest warm and wet airflow	Anthropogenic aerosol emission	Aggregation (precipitation become more concentrated; the central value becomes stronger)	Liu et al. (2019)
e	Beijing	21 Jul 2012	25.9°C	86.5%	Vortices, troughs, cold fronts, low-level jets with sufficient moisture	Land cover change, anthropogenic heat	Aggregation (spatial distribution become more concentrated)	Yu and Li (2015)
f	Beijing	21 Jul 2012	25.9°C	86.5%	The same as above	Land cover change	Weak (recent high urban development caused no significant change of precipitation)	Wang et al. (2015)
g	Beijing	19 Jul 2016	23.8°C	87.0%	Cold vortex, low-level jet, and monsoon system	Anthropogenic aerosol emission	Inhibition (suppressed precipitation intensity)	Guo et al. (2019)
h	Xiong'an	20 Jul 2016	23.9°C	95.0%	Cold vortex, low-level jet, and monsoon system	Land cover change	Aggregation (convective activity increased and rainfall in downwind area enhanced)	Xing et al. (2019)
i	Yangtze River delta	5 Jul 2003	27.6°C	83.8%	Southwesterly monsoon	Land cover change	Weak (rainfall slightly increase in the downwind of the city belt and decrease in the upwind)	Wan et al. (2013)
j	Yangtze River delta	24 Jun 2006	27.5°C	80.4%	Strong winds and large spatial convergence	Land cover change, aerosol emission	Inhibition (suppresses precipitation)	Zhong et al. (2017)
k	Beijing	4 Jun 2003	23.5°C	63.8%	Convective cloud system	Land cover change	Aggregation (precipitation become more concentrated and intensified)	Guo et al. (2006)
l	Beijing	1 Aug 2006	25.2°C	73.4%	Weak synoptic forcing	Land cover change, anthropogenic heat	Aggregation (rainfall become more locally concentrated)	Miao et al. (2011)
m	Shanghai	13 Sep 2013	27.8°C	79.6%	Convective process	Land cover change	Aggregation (precipitation become more concentrated)	Zhang et al. (2017)
n	Yangtze River delta	2 Jul 2006	29.0°C	77.6%	Weak synoptic forcing	Land cover change, aerosol emission	Aggregation (enhances the convergence of moisture fluxes)	Zhong et al. (2017)

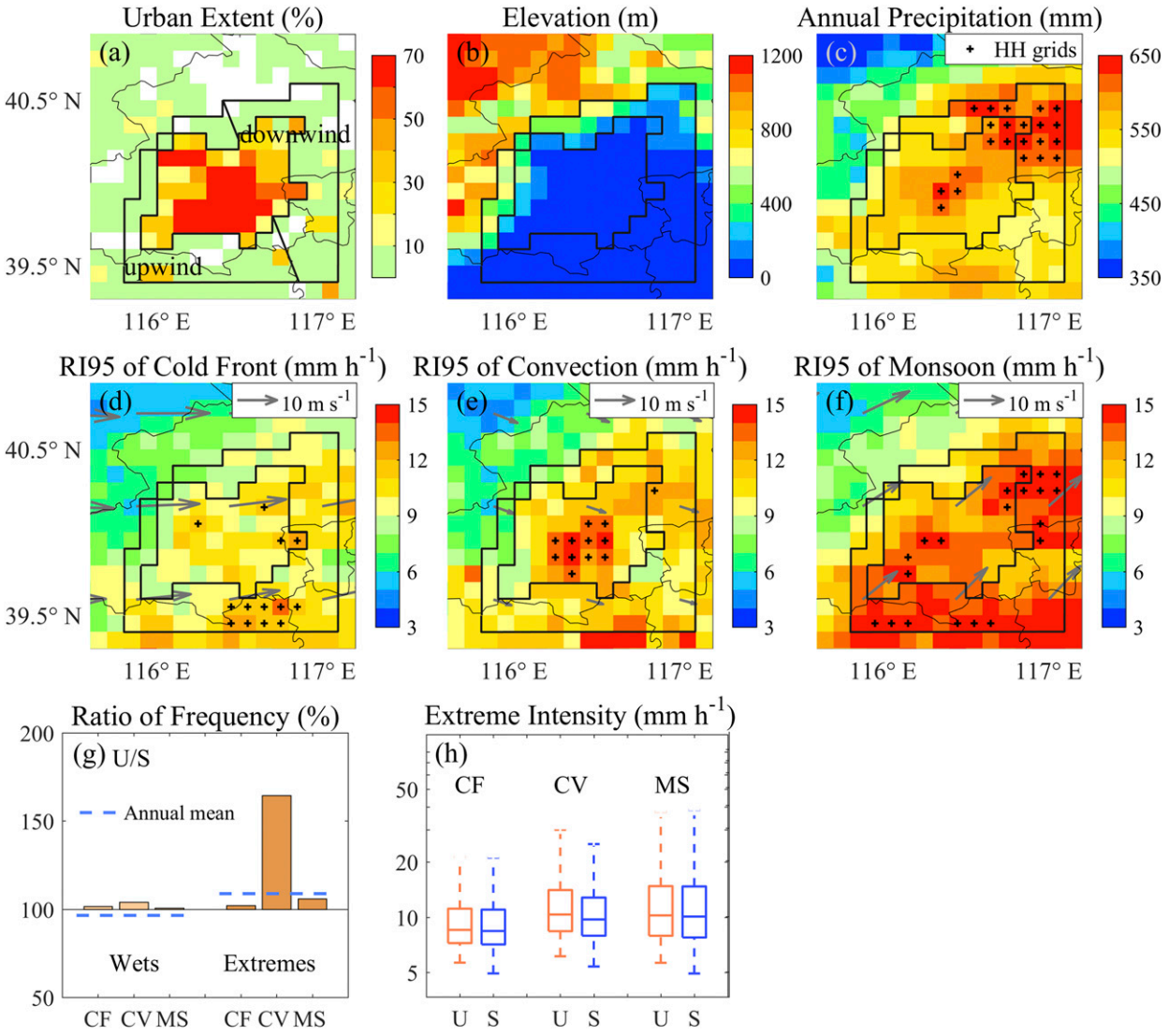

FIG. 7. Spatial distribution of (a) urban extent (%), (b) elevation (m), (c) annual mean precipitation (mm), and (d)–(f) the mean intensities (mm h^{-1}) of RI95 for cold frontal precipitation (CF), convective precipitation (CV), and summer monsoon precipitation (MS) over the Beijing domain. (g) Precipitation ratio for the frequency of wets (>0.1 mm h^{-1}) and extremes (≥16 mm h^{-1}) between urban (U) and suburban (S) areas, and (h) the boxplot of precipitation intensity (≥95th percentile) over urban and suburban areas among the three cluster types. The urban grids and the surrounding suburban grids are outlined, and the suburban region is divided into the climatological upwind (southwest) and downwind (northeast) areas according to the climatic wind direction. Grids in the significant HH cluster (with a 95% confidence level) are marked with + symbols in (c)–(f).

fewer rainy hours, 36% more extreme rainy hours, and 2.5 mm h^{-1} higher rainfall intensities than the surrounding suburban areas (Figs. 8h,i). Southwesterly monsoon precipitation spans from May to June. It accounts for 17.5% of the total days while contributes 39% (42%) of the annual mean precipitation and 47% (54%) of extremes in the urban (suburban) areas (Table 4). In contrast, the convection precipitation has more annual extreme precipitation (33.1 versus 23.2 mm $grid^{-1}$), more extreme precipitation hours (24% more) and higher intensities (14.3 versus 12.8 mm h^{-1}) in the urban area than the suburb (Figs. 8h,i and Table 4). The typhoon events represent anticlockwise wind, and the spatial pattern of typhoon-related precipitation is less correlated with the urban extent (Fig. 8g). The grids in significant HH clusters for cold frontal and convection systems match well with the urban center of Guangzhou, Dongguan, and Shenzhen, indicating that the urban areas in the PRD mainly affect the spatial clustering of precipitation extremes for these two types. We further investigate how the synoptic background influences the urban signature in spatial clustering of precipitation extremes.

2) INFLUENCES OF AIR TEMPERATURE AND RH

The statistical analysis examines the hypothesis that the urban signatures in spatial clustering of precipitation extremes

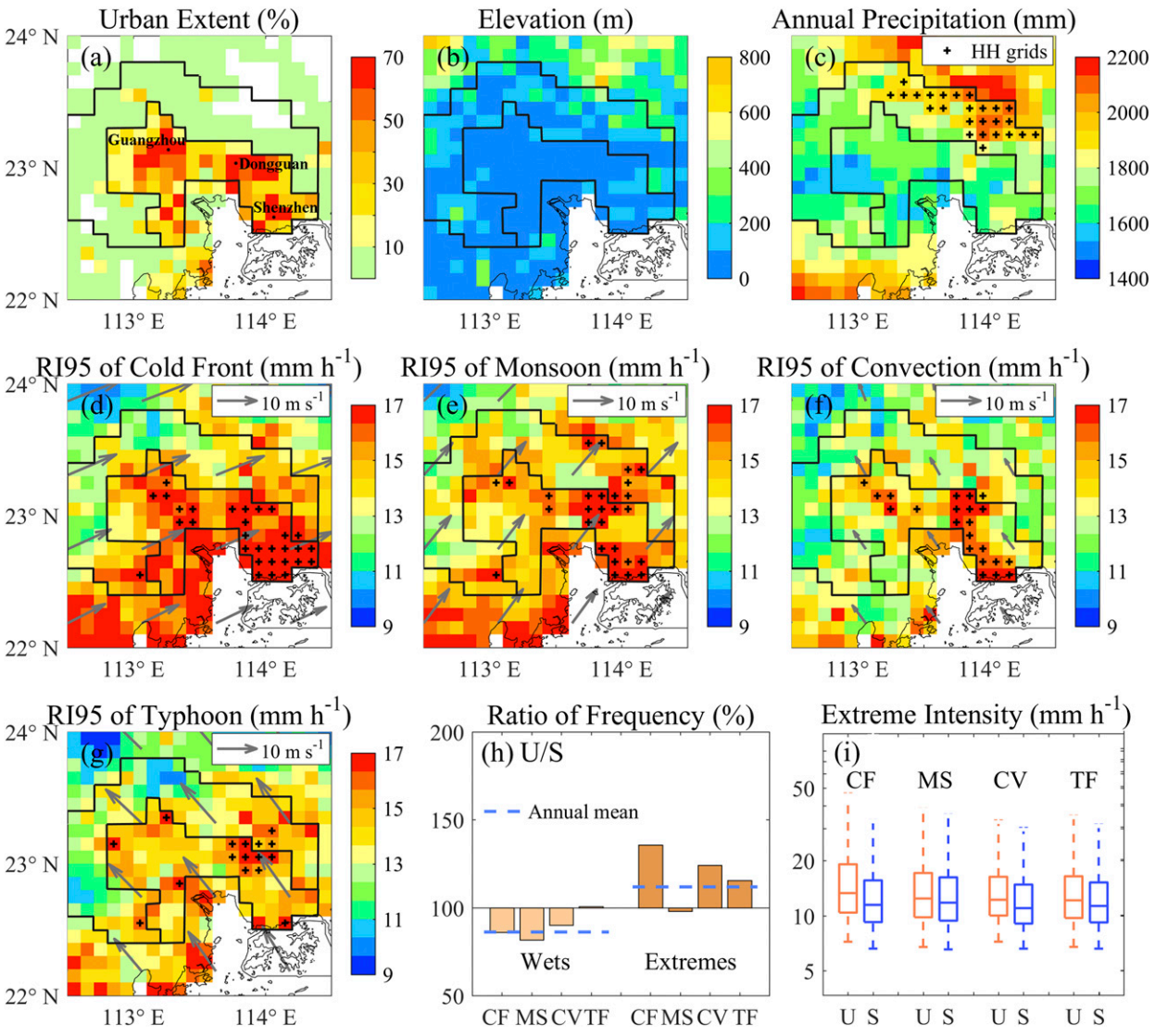

FIG. 8. As in Fig. 7, but for the cold frontal precipitation (CF), monsoon precipitation (MS), convective precipitation (CV), and the typhoon precipitation (TF) over the PRD domain.

vary with different synoptic background and the related precipitation types. We further investigate the favorable synoptic conditions of urban effects on spatial clustering of precipitation extremes by examining the relationship of the areal mean temperature and RH against the heterogeneity patterns of extreme precipitation at a daily scale in the Beijing and PRD areas (Figs. 9 and 10). The extreme days were defined as days that at least five grids have hourly precipitation records exceeds their 95th percentile threshold during the study period. The spatial distribution of the accumulated precipitation in each extreme day was selected for the LISA analysis and was characterized into HU days, LU days, or MIX days, and the corresponding areal mean temperature and RH in each extreme day were identified using the CLDAS data.

In Beijing, HU days take up 32%, 54%, and 53% of the extreme days under the three synoptic conditions (Figs. 9a–c). Generally, HU days and LU days have similar probability distribution functions with temperature for extreme precipitation in the frontal and monsoon systems (Figs. 9d,f). In contrast, HU has a higher probability of around 25°–27°C and in humid conditions (RH > 75%) than LU for the convection extreme precipitation, and LU has a much higher probability than HU as RH < 70% (Figs. 9e,h).

In the PRD, it has more extreme days, higher temperature, and higher RH than Beijing. HU (LU) holds 51% (42%), 41% (54%), and 53% (43%) of the extreme days under the three synoptic conditions of cold front, warm monsoon and convective precipitation (Fig. 10). HU tends to occur in moderate temperature (between 20° and 24°C) and high RH (>85%) for the humid cold frontal systems (Figs. 10d,g). Besides, HU has a higher probability above 28°C and in lower RH ranges (75%–85%) than LU for the convection extreme precipitation

TABLE 3. Proportions of precipitation and the Moran's *I* values of extreme indices for each cluster type over the Beijing domain. Extreme precipitation is defined as hourly rainfall with an intensity exceeding 16 mm h^{-1}.

		Humid winter	Dry winter	Cold front	Convection	Monsoon
Proportion of total days (%)		26.6%	15.0%	18.6%	25.5%	14.3%
Proportion of total precipitation (%)		2.1%	0.8%	36.2%	10.0%	50.9%
Annual mean precipitation (mm $grid^{-1}$)	Urban	11.8	3.6	203.3	59.1	291.7
	Suburban	12.0	4.8	202.9	54.1	281.3
	Upwind	11.3	4.9	204.0	53.9	267.9
	Downwind	12.8	4.7	201.7	54.3	294.7
Annual mean extreme precipitation (mm $grid^{-1}$)	Urban	—	—	7.8	7.1	60.4
	Suburban	—	—	7.9	4.7	59.1
	Upwind	—	—	9.3	5.1	54.3
	Downwind	—	—	6.4	4.4	63.9
Moran's *I* of RI95		—	—	0.19	0.47	0.41

(Figs. 10f,i). Both HU and LU demonstrate a similar probability pattern against temperature and RH for the monsoon precipitation extremes (Figs. 10e,h).

Even though differences exist in the specific ranges for different regions, the results suggest that precipitation extremes are likely to be clustered over urban areas (HU) within two *T*–RH ranges. One is in high temperature and lower RH ranges (Figs. 9b and 10c), and another is in moderate temperature and high RH ranges (Fig. 10a). In other words, urban effect on precipitation extremes may become more prominent in warmer (benefit for local convention) or wetter (humid frontal systems) conditions.

3) INTEGRATED ANALYSIS

Though no global picture emerges for the urban signatures of precipitation extremes among all events and synoptic backgrounds, it is observed that the urban signatures is more prominent in warmer or wetter conditions at an event scale (Figs. 9 and 10). The urban effects on precipitation heterogeneity can be categorized in three conditions when extreme precipitation events occur (Fig. 11): phase I in moderate temperature and high RH range, phase II in high temperature and moderate RH range, and phase III in high temperature and low RH range. At an event scale, both thermodynamic and dynamic factors could affect the moisture capacity, redistribute the moisture in a storm, and trigger ascending motion, resulting in changes of precipitation structures and intensities (Drobinski et al. 2016). The different role of urban environment in modulating storm dynamics and precipitation efficiency under different synoptic backgrounds could explain the spatial clustering pattern of precipitation extremes over urban-affected areas in different condition.

In phase I, the urban modification on precipitation pattern is remarkable under conditions with sufficient water supply, which mainly occurs in April and May in south China (Su et al. 2019), e.g., in the no water-limited cold frontal system over the PRD region (Figs. 8d and 10g). Urban surface features can provide favorable conditions for deep convections by modifying the level of free convection (LFC) and boundary layer height. Higher temperature over urban areas could hold more water vapor, promote greater moisture convergence and allow the air rise sooner to the LFC than colder areas, which finally enhance the intensity and total amount of heavy rainfall events over urban areas (Trenberth et al. 2003). Furthermore, the urban roughness effects could slow the cold front movement, thus delaying the full development of the precipitation system (Huang et al. 2019). In the humid frontal system, urban forcing may not be a constraining factor for the initiation and development of deep convection, but urban effects do influence the timing and location of precipitation events and benefit the aggregation of spatial heterogeneity.

In phase II, the urban effect is relatively weak in a strong synoptic background, which is associated with the large-scale monsoon rainfall and typhoon-related rainfall that affect most areas of China. The large-scale synoptic system may weaken the local wind convergence and strengthen the moisture advection, resulting in a weaker local UHI circulation, such as the typhoon precipitation (Fig. 8g). Besides, multiple dynamic processes like frontal lifting, orographic lifting, and sea–land breeze could provide the energy to overcome the convective inhibition (CIN). It is evident that the windward side of mountainous areas and the urban areas are the clustered regions of precipitation extremes in frontal systems (e.g., the

TABLE 4. As in Table 3, but for the PRD domain.

		Humid winter	Dry winter	Cold front	Monsoon	Convection	Typhoon
Proportion of total days (%)		10.7%	18.0%	29.6%	17.5%	20.1%	4.1%
Proportion of total precipitation (%)		5.6%	4.8%	17.1%	40.8%	14.0%	17.7%
Annual mean precipitation (mm $grid^{-1}$)	Urban	91.2	74.3	288.6	655.4	245.0	322.0
	Suburban	100.0	90.2	303.9	747.9	242.8	296.9
Annual mean extreme precipitation (mm $grid^{-1}$)	Urban	4.1	—	57.9	133.9	33.1	55.7
	Suburban	3.7	—	40.5	137.8	23.2	45.9
Moran's *I* of RI95		0.49	—	0.78	0.51	0.54	0.61

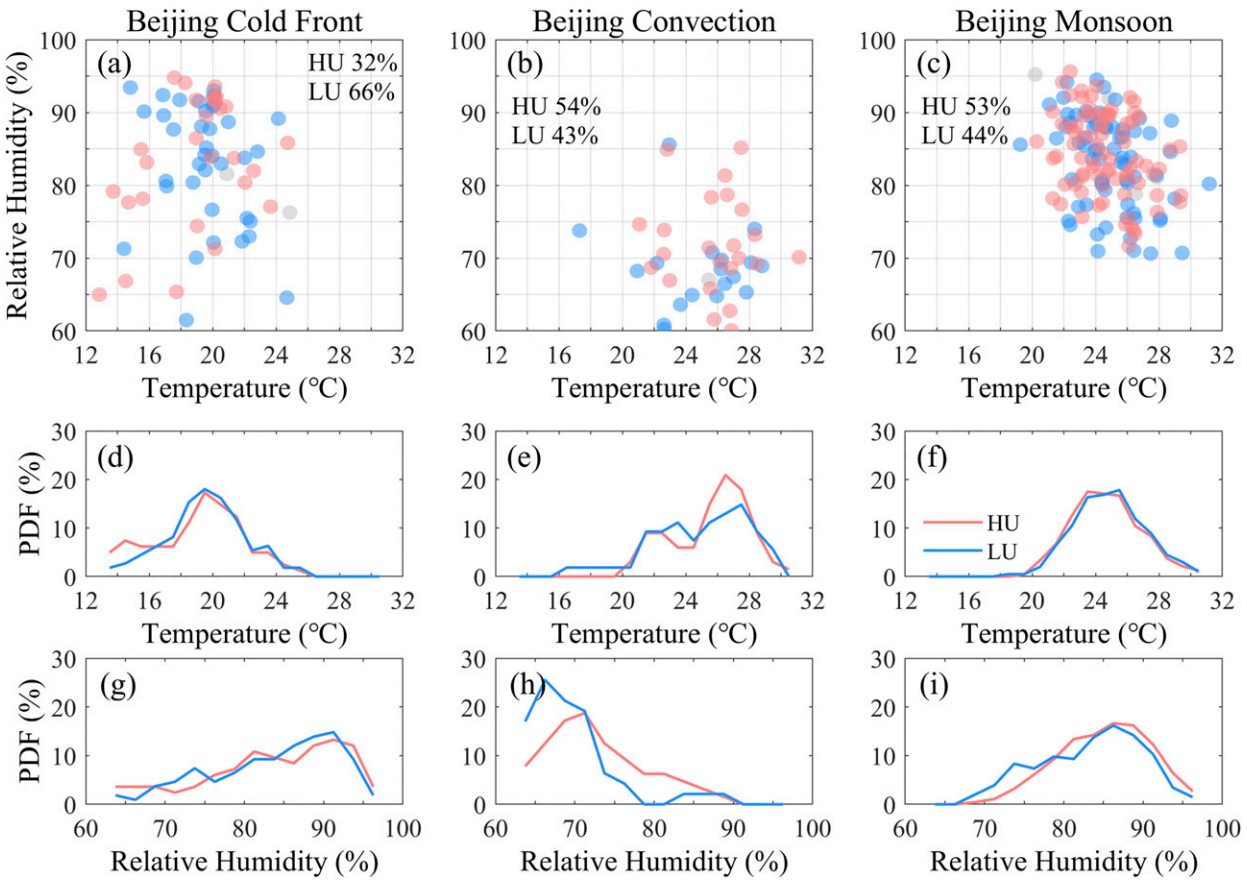

FIG. 9. (a)–(c) Scatterplot for HU (red), LU (blue), and MIX (gray) extreme days with the corresponding areal mean temperature and relative humidity for the three cluster types over the Beijing domain; the proportions of total HU and LU days in each cluster are listed. (d)–(i) Probability distribution function of HU days and LU days against temperature and relative humidity.

monsoon precipitation of Beijing and PRD, Figs. 7f and 8e). In these cases, the urban-induced processes could be of less importance, and the differences in the frequency/intensity of extreme precipitation over the urban and suburban areas are not significant (Figs. 7g,h and 8h,i).

In phase III, the urban effect becomes dominant by promoting moisture convergence and vertical motions when the synoptic forcing is relatively weak and the air temperature is high (Figs. 7e and 8f). The surface temperature peaks in the afternoon due to the solar radiation and surface thermal radiation; the unstable energy could last to the evening. The UHI and increased surface roughness favor local moisture convergence in the lower atmosphere, the urban-induced sensible heat flux and thermodynamic turbulent flow could promote vertical motions and trigger local convective systems (Han et al. 2014). As a result, more frequent and intense extreme precipitation occurred over the urban areas during summer (e.g., convective precipitation of Beijing and PRD, Figs. 7e and 8f), especially in the afternoon.

The effects of urbanization on precipitation pattern and extremes have been tested based on numerical modeling in many case studies, but synthesized information to reveal the urban signatures in modifying the spatial heterogeneity pattern of precipitation extremes under different synoptic conditions is scare. In this study, results of 14 modeling case studies over several metropolitans in mainland China were systematically reviewed. The description of the synoptic condition of each event as well as the heterogeneity change of precipitation extremes after urbanization were summarized in Table 2. The corresponding daily mean temperature and RH of these events were also calculated and showed in the schematic drawing of Fig. 11. The *T*–RH ranges of the three phases were roughly summarized from the analyses in Beijing and the PRD (Figs. 9 and 10). Generally, the related urban signatures in the spatial clustering of precipitation extremes are consistent with the results of previous modeling studies (Fig. 11 and Table 2). Urban areas play a crucial role in the spatial clustering of precipitation extremes (in frequency, intensity, and amount) for the humid frontal systems (phase I; Zhong and Yang 2015; Huang et al. 2019; Liu et al. 2019) and the convective cloud system with relative weak large-scale synoptic forcing (phase III; Guo et al. 2006; Miao et al. 2011; Zhang et al. 2017; Zhong et al. 2017). In a strong synoptic background (phase II), the combined effects of multiple dynamic factors on precipitation are complex and depend on specific condition in each event, resulting in aggregation (Yu and Liu 2015; Xing et al. 2019), inhibition (Zhong et al. 2017; Guo et al. 2019), or very weak

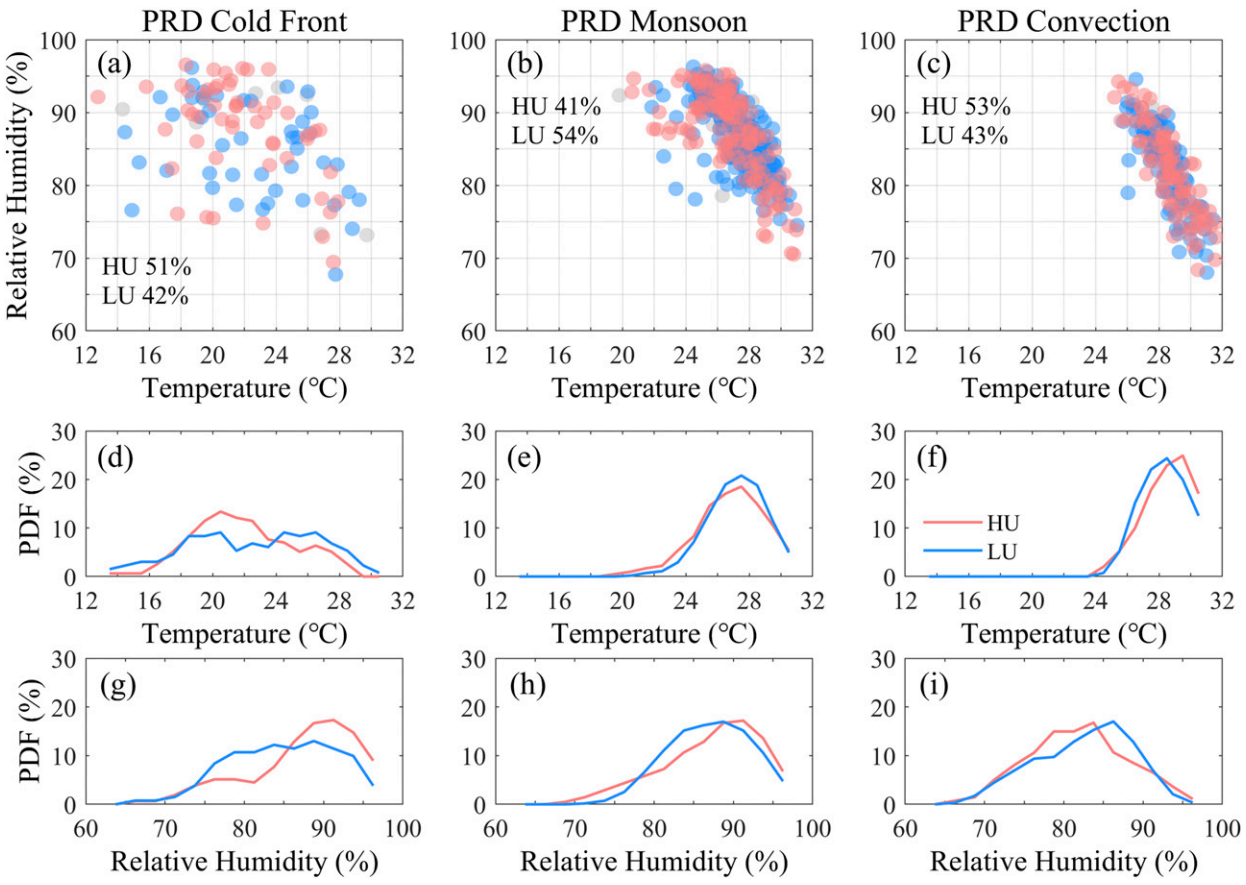

FIG. 10. As in Fig. 9, but for the extreme days over the PRD domain.

(Wan et al. 2013; Wang et al. 2015) effects of urbanization on the precipitation clustering. Furthermore, the inconsistent results in different modeling studies on the same event (e.g., Yu and Liu 2015; Wang et al. 2015) imply the large uncertainty in simulating the effects of urbanization on heavy precipitation by different approaches and model configurations. Overall, our understanding of urban effects on the spatial clustering of precipitation events is far from clarity, especially for heavy events under strong synoptic forcing.

4. Summary

This study presents the urban signatures in the spatial heterogeneity patterns of precipitation intensity over 130 cities in mainland China using a merged high-resolution precipitation dataset. The roles of urban extent and underlying mechanisms on the observed spatial clustering of precipitation extremes are further investigated and discussed in the Beijing and PRD domains under different synoptic conditions. The primary conclusions are summarized below.

1) The spatial clustering patterns of precipitation over the UARs are not universal across mainland China. Only 37 cities (28%) are observed with significant urban signatures on the spatial clustering of precipitation extremes. The impact of the urban extent on the clustering of precipitation is associated with urban sizes (The HU takes up 43% RI95 in the grade 1 cities, but only 24% in the grade 2 cities). Extreme and heavy precipitation has higher spatial clustering than light precipitation (mean Moran's I = 0.49, 0.47, and 0.37, respectively).
2) The spatial clustering of precipitation varies distinctly in different geographic regions, which is largely determined by the local climate setting and topography. The Haihe River basin, the Yangtze River basin and the Pearl River basin are typical regions with urban signatures (HU dominates with the proportion of 44%, 48%, and 36%, respectively).
3) The urban signature on the spatial clustering of precipitation extremes varies with synoptic conditions and their related precipitation types, and is predominant for local convective precipitation in Beijing (Moran's I = 0.47) and for the cold frontal precipitation in the PRD area (Moran's I = 0.78).
4) Precipitation efficiency and regional dynamics are the strong drivers for the spatial clustering of precipitation extremes, and the urban effect tends to be more prominent in warmer (>25°C over Beijing and >28°C over the PRD) or wetter (>75% over Beijing and >85% over the PRD) conditions.

Our study highlights the urban signatures in forming the spatial clustering of some precipitation extremes. However,

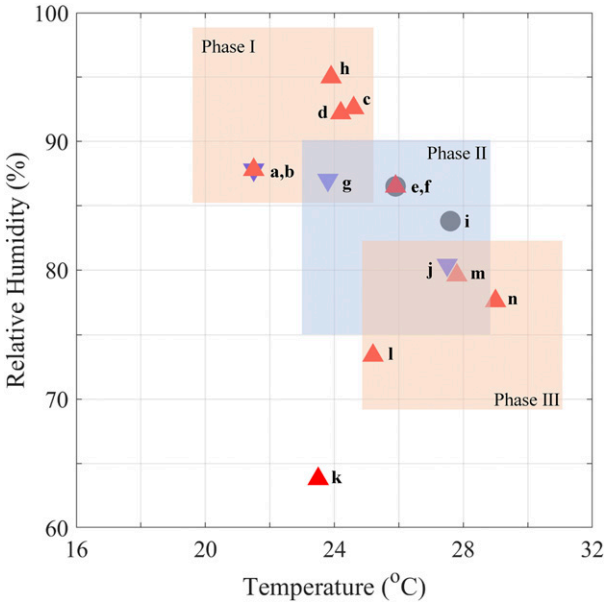

FIG. 11. A schematic drawing of the temperature–RH ranges for the different urban signatures in spatial clustering of local precipitation extremes. Fourteen modeling case studies (details are listed in Table 2) are illustrated with the corresponding daily mean temperature and RH. The upward triangle, downward triangle, and the circle represent the effects of local urbanization on the spatial clustering of precipitation events are aggregation, inhibition, and have weak influence, respectively.

uncertainties and limitations may exist due to the short record length and the unsupervised classification method in classifying synoptic backgrounds. Besides, mechanisms of the urban effects in the spatial clustering of precipitation extremes have not been fully understood. Further observation and modeling studies on more events under different synoptic conditions and impact factors are needed to reveal the role of urban areas on the spatial clustering of precipitation and the related mechanisms, such as accurate divisions of precipitation types, land cover and land use change, anthropogenic heat, anthropogenic aerosol emission, and so on. That is what we are currently working on but beyond the scope of this manuscript.

This work is a successful attempt in linking the spatial heterogeneity patterns of precipitation extremes and urban effects in mainland China. This study presents the spatial heterogeneity features of precipitation at the urban scale and their regional variations, and investigates the favorable synoptic conditions and probably temperature and relative humidity ranges of urban effects on individual events. The observed clustered extreme rainfall over urbanized areas is likely to cause hydrologic hazards and stress water availability. Cities may suffer from increasingly clustered precipitation extremes in the future due to the combined effects of climate change and urbanization. Therefore, it is strongly encouraged to take precautions and adaptation strategies to mitigate the adverse effect of the highly concentrated extreme rainfall events, particularly in the urban areas located in the Haihe River basin, the Yangtze River basin, and the Pearl River basin of China.

Acknowledgments. This study is funded by the National Natural Science Foundation of China (42001321, 41871085, 51779278), and the China Postdoctoral Science Foundation (2020M672693). We thank all the researchers and staff for providing and maintaining the meteorological data and land cover data from all agencies.

Data availability statement. All data used in this study are accessed from the following links. CMPA: http://www.nmic.cn/data/cdcdetail/dataCode/SEVP_CLI_CHN_MERGE_CMP_PRE_HOUR_GRID_0.10.html; JRA-55 reanalysis data: http://jra.kishou.go.jp/JRA-55/index_en.html; CLDAS: http://www.nmic.cn/data/cdcdetail/dataCode/NAFP_CLDAS2.0_RT.html; LULC, boundary of administrative districts and basins, centre of prefecture-level cities: http://www.resdc.cn/ (the Resource and Environment Data Cloud Platform of Chinese Academy of Sciences).

REFERENCES

Anselin, L., 1995: Local indicators of spatial association—LISA. *Geogr. Anal.*, **27**, 93–115, https://doi.org/10.1111/j.1538-4632.1995.tb00338.x.

Ashley, W. S., M. L. Bentley, and J. A. Stallins, 2012: Urban-induced thunderstorm modification in the southeast United States. *Climatic Change*, **113**, 481–498, https://doi.org/10.1007/s10584-011-0324-1.

Bloom, D. E., 2011: 7 billion and counting. *Science*, **333**, 562–569, https://doi.org/10.1126/science.1209290.

Chen, G., T. Iwasaki, H. Qin, and W. Sha, 2014: Evaluation of the warm-season diurnal variability over East Asia in recent reanalyses JRA-55, ERA-Interim, NCEP CFSR, and NASA MERRA. *J. Climate*, **27**, 5517–5537, https://doi.org/10.1175/JCLI-D-14-00005.1.

Chen, S., and Coauthors, 2016: Precipitation spectra analysis over China with high-resolution measurements from optimally-merged satellite/gauge observations—Part I: Spatial and seasonal analysis. *IEEE J. Sel. Topics Appl. Earth Obs. Remote Sens.*, **9**, 2966–2978, https://doi.org/10.1109/JSTARS.2016.2529003.

Dai, A., X. Lin, and K. Hsu, 2007: The frequency, intensity, and diurnal cycle of precipitation in surface and satellite observations over low- and mid-latitudes. *Climate Dyn.*, **29**, 727–744, https://doi.org/10.1007/s00382-007-0260-y.

Deng, Y., T. Gao, H. Gao, X. Yao, and L. Xie, 2014: Regional precipitation variability in East Asia related to climate and environmental factors during 1979-2012. *Sci. Rep.*, **4**, 5693, https://doi.org/10.1038/srep05693.

Drobinski, P., B. Alonzo, S. Bastin, N. D. Silva, and C. Muller, 2016: Scaling of precipitation extremes with temperature in the French Mediterranean region: What explains the hook shape? *J. Geophys. Res. Atmos.*, **121**, 3100–3119, https://doi.org/10.1002/2015JD023497.

Feddema, J. J., K. W. Oleson, G. B. Bonan, L. O. Mearns, L. E. Buja, G. A. Meehl, and W. M. Washington, 2005: The importance of land-cover change in simulating future climates. *Science*, **310**, 1674–1678, https://doi.org/10.1126/science.1118160.

Fu, X., X. Yang, and X. Sun, 2019: Spatial and diurnal variations of summer hourly rainfall over three super city clusters in Eastern China and their possible link to the urbanization. *J. Geophys. Res. Atmos.*, **124**, 5445–5462, https://doi.org/10.1029/2019JD030474.

Georgescu, M., A. Mahalov, and M. Moustaoui, 2012: Seasonal hydroclimatic impacts of Sun Corridor expansion. *Environ. Res. Lett.*, **7**, 034026, https://doi.org/10.1088/1748-9326/7/3/034026.

Ghosh, S., D. Das, S. C. Kao, and A. R. Ganguly, 2012: Lack of uniform trends but increasing spatial variability in observed Indian rainfall extremes. *Nat. Climate Change*, **2**, 86–91, https://doi.org/10.1038/nclimate1327.

Gu, X., Q. Zhang, J. Li, V. P. Singh, and P. Sun, 2019: Impact of urbanization on nonstationarity of annual and seasonal precipitation extremes in China. *J. Hydrol.*, **575**, 638–655, https://doi.org/10.1016/j.jhydrol.2019.05.070.

Guo, C., H. Xiao, H. Yang, and W. Wen, 2019: Effects of anthropogenic aerosols on a heavy rainstorm in Beijing. *Atmosphere*, **10**, 162, https://doi.org/10.3390/atmos10040162.

Guo, X., D. Fu, and J. Wang, 2006: Mesoscale convective precipitation system modified by urbanization in Beijing City. *Atmos. Res.*, **82**, 112–126, https://doi.org/10.1016/j.atmosres.2005.12.007.

Han, J. Y., J. J. Baik, and H. Lee, 2014: Urban impacts on precipitation. *Asia-Pac. J. Atmos. Sci.*, **50**, 17–30, https://doi.org/10.1007/s13143-014-0016-7.

Huang, Y., Y. Liu, Y. Liu, H. Li, and J. C. Knievel, 2019: Mechanisms for a record-breaking rainfall in the coastal metropolitan city of Guangzhou, China: Observation analysis and nested very large eddy simulation with the WRF model. *J. Geophys. Res. Atmos.*, **124**, 1370–1391, https://doi.org/10.1029/2018JD029668.

Huff, F. A., and S. A. Changnon Jr., 1973: Precipitation modification by major urban areas. *Bull. Amer. Meteor. Soc.*, **54**, 1220–1232, https://doi.org/10.1175/1520-0477(1973)054<1220:PMBMUA>2.0.CO;2.

Joyce, R. J., J. E. Janowiak, P. A. Arkin, and P. P. Xie, 2004: CMORPH: A method that produces global precipitation estimates from passive microwave and infrared data at high spatial and temporal resolution. *J. Hydrometeor.*, **5**, 487–503, https://doi.org/10.1175/1525-7541(2004)005<0487:CAMTPG>2.0.CO;2.

Kaufmann, R. K., K. C. Seto, A. Schneider, Z. Liu, L. Zhou, and W. Wang, 2007: Climate response to rapid urban growth: Evidence of a human-induced precipitation deficit. *J. Climate*, **20**, 2299–2306, https://doi.org/10.1175/JCLI4109.1.

Kobayashi, S., and Coauthors, 2015: The JRA-55 reanalysis: General specifications and basic characteristics. *J. Meteor. Soc. Japan*, **93**, 5–48, https://doi.org/10.2151/jmsj.2015-001.

Li, W., S. Cheng, G. Chen, W. Sha, C. Luo, Y. Feng, Z. Wen, and B. Wang, 2011: Urbanization signatures in strong versus weak precipitation over the Pearl River Delta metropolitan regions of China. *Environ. Res. Lett.*, **6**, 034020, https://doi.org/10.1088/1748-9326/6/3/034020.

Liu, C., T. Wang, P. Chen, M. Li, M. Zhao, K. Zhao, M. H. Wang, and X. Q. Yang, 2019: Effects of aerosols on the precipitation of convective clouds: A case study in the Yangtze River Delta of China. *J. Geophys. Res. Atmos.*, **124**, 7868–7885, https://doi.org/10.1029/2018JD029924.

Liu, J., M. Liu, H. Tian, D. Zhuang, Z. Zhang, W. Zhang, X. Tang, and X. Deng, 2005: Spatial and temporal patterns of China's cropland during 1990–2000: An analysis based on Landsat TM data. *Remote Sens. Environ.*, **98**, 442–456, https://doi.org/10.1016/j.rse.2005.08.012.

Luo, M., and N. Lau, 2018: Increasing heat stress in urban areas of Eastern China: Acceleration by urbanization. *Geophys. Res. Lett.*, **45**, 13 060–13 069, https://doi.org/10.1029/2018GL080306.

Miao, C., Q. Sun, A. G. Borthwick, and Q. Duan, 2016: Linkage between hourly precipitation events and atmospheric temperature changes over China during the warm season. *Sci. Rep.*, **6**, 22543, https://doi.org/10.1038/srep22543.

Miao, S., F. Chen, Q. Li, and S. Fan, 2011: Impacts of urban processes and urbanization on summer precipitation: A case study of heavy rainfall in Beijing on 1 August 2006. *J. Appl. Meteor. Climatol.*, **50**, 806–825, https://doi.org/10.1175/2010JAMC2513.1.

Moran, P. A. P., 1950: Notes on continuous stochastic phenomena. *Biometrika*, **37**, 17–23, https://doi.org/10.1093/biomet/37.1-2.17.

Mote, T. L., M. C. Lacke, and J. M. Shepherd, 2007: Radar signatures of the urban effect on precipitation distribution: A case study for Atlanta, Georgia. *Geophys. Res. Lett.*, **34**, L20710, https://doi.org/10.1029/2007GL031903.

Niyogi, D., P. Pyle, M. Lei, S. P. Arya, C. M. Kishtawal, M. Shepherd, F. Chen, and B. Wolfe, 2011: Urban modification of thunderstorms: An observational storm climatology and model case study for the Indianapolis urban region. *J. Appl. Meteor. Climatol.*, **50**, 1129–1144, https://doi.org/10.1175/2010JAMC1836.1.

Pielke, R. A., and Coauthors, 2011: Land use/land cover changes and climate: Modeling analysis and observational evidence. *Wiley Interdiscip. Rev.: Climate Change*, **2**, 828–850, https://doi.org/10.1002/wcc.144.

Prat, O. P., and B. R. Nelson, 2013: Mapping the world's tropical cyclone rainfall contribution over land using the TRMM Multi-satellite Precipitation Analysis. *Water Resour. Res.*, **49**, 7236–7254, https://doi.org/10.1002/wrcr.20527.

Ren, G., 2015: Urbanization as a major driver of urban climate change. *Adv. Climate Change Res.*, **6**, 1–6, https://doi.org/10.1016/j.accre.2015.08.003.

Renard, F., 2017: Local influence of south-east France topography and land cover on the distribution and characteristics of intense rainfall cells. *Theor. Appl. Climatol.*, **128**, 393–405, https://doi.org/10.1007/s00704-015-1698-1.

Rosenfeld, D., U. Lohmann, G. B. Raga, C. D. Odowd, M. Kulmala, S. Fuzzi, A. Reissell, and M. O. Andreae, 2008: Flood or drought: How do aerosols affect precipitation? *Science*, **321**, 1309–1313, https://doi.org/10.1126/science.1160606.

Schmid, P. E., and D. Niyogi, 2013: Impact of city size on precipitation-modifying potential. *Geophys. Res. Lett.*, **40**, 5263–5267, https://doi.org/10.1002/grl.50656.

Shastri, H., S. Paul, S. Ghosh, and S. Karmakar, 2015: Impacts of urbanization on Indian summer monsoon rainfall extremes. *J. Geophys. Res. Atmos.*, **120**, 496–516, https://doi.org/10.1002/2014JD022061.

——, S. Ghosh, and S. Karmakar, 2017: Improving Global Forecast System of extreme precipitation events with regional statistical model: Application of quantile-based probabilistic forecasts. *J. Geophys. Res. Atmos.*, **122**, 1617–1634, https://doi.org/10.1002/2016JD025489.

Shen, Y., P. Zhao, Y. Pan, and J. Yu, 2014: A high spatiotemporal gauge-satellite merged precipitation analysis over China. *J. Geophys. Res. Atmos.*, **119**, 3063–3075, https://doi.org/10.1002/2013JD020686.

Shepherd, J. M., M. Carter, M. Manyin, D. Messen, and S. Burian, 2010: The impact of urbanization on current and future coastal precipitation: A case study for Houston. *Environ. Plann.*, **37B**, 284–304, https://doi.org/10.1068/b34102t.

Shi, C. X., Z. H. Xie, H. Qian, M. L. Liang, and X. C. Yang, 2011: China land soil moisture EnKF data assimilation based on satellite remote sensing data. *Sci. China Earth Sci.*, **54**, 1430–1440, https://doi.org/10.1007/s11430-010-4160-3.

Singh, J., H. Vittal, S. Karmakar, S. Ghosh, and D. Niyogi, 2016: Urbanization causes nonstationarity in Indian summer monsoon

rainfall extremes. *Geophys. Res. Lett.*, **43**, 11 269–11 277, https://doi.org/10.1002/2016GL071238.

Su, L., J. Li, X. Shi, and J. C. Fung, 2019: Spatiotemporal variation in presummer precipitation over south China from 1979 to 2015 and its relationship with urbanization. *J. Geophys. Res. Atmos.*, **124**, 6737–6749, https://doi.org/10.1029/2019JD030751.

Sun, Q., C. Miao, and Q. Duan, 2017: Changes in the spatial heterogeneity and annual distribution of observed precipitation across China. *J. Climate*, **30**, 9399–9416, https://doi.org/10.1175/JCLI-D-17-0045.1.

Tang, G., D. Long, and Y. Hong, 2016: Systematic anomalies over inland water bodies of high mountain Asia in TRMM precipitation estimates: No longer a problem for the GPM era? *IEEE Geosci. Remote Sens.*, **13**, 1762–1766, https://doi.org/10.1109/LGRS.2016.2606769.

Trenberth, K. E., A. Dai, R. M. Rasmussen, and D. B. Parsons, 2003: The changing character of precipitation. *Bull. Amer. Meteor. Soc.*, **84**, 1205–1218, https://doi.org/10.1175/BAMS-84-9-1205.

Wan, H., Z. Zhong, X. Yang, and X. Li, 2013: Impact of city belt in Yangtze River Delta in China on a precipitation process in summer: A case study. *Atmos. Res.*, **125–126**, 63–75, https://doi.org/10.1016/j.atmosres.2013.02.004.

Wang, D. S., D. G. Wang, X. Qi, L. Liu, and X. W. Wang, 2018: Use of high-resolution precipitation observations in quantifying the effect of urban extent on precipitation characteristics for different climate conditions over the Pearl River Delta, China. *Atmos. Sci. Lett.*, **19**, e820, https://doi.org/10.1002/asl.820.

——, X. W. Wang, L. Liu, D. G. Wang, H. B. Huang, and C. L. Pan, 2019: Evaluation of TMPA 3B42V7, GPM IMERG and CMPA precipitation estimates in Guangdong Province, China. *Int. J. Climatol.*, **39**, 738–755, https://doi.org/10.1002/joc.5839.

Wang, J., J. Feng, Z. Yan, Y. Hu, and G. Jia, 2012: Nested high-resolution modeling of the impact of urbanization on regional climate in three vast urban agglomerations in China. *J. Geophys. Res.*, **117**, D21103, https://doi.org/10.1029/2012JD018226.

——, ——, and ——, 2015: Potential sensitivity of warm season precipitation to urbanization extents: Modeling study in Beijing-Tianjin-Hebei urban agglomeration in China. *J. Geophys. Res. Atmos.*, **120**, 9408–9425, https://doi.org/10.1002/2015JD023572.

Xing, Y., G. Ni, L. Yang, Y. Yang, P. Xing, and T. Sun, 2019: Modeling the impacts of urbanization and open water surface on heavy convective rainfall: A case study over the emerging Xiong'an City, China. *J. Geophys. Res. Atmos.*, **124**, 9078–9098, https://doi.org/10.1029/2019JD030359.

Yang, L., F. Tian, J. A. Smith, and H. Hu, 2014: Urban signatures in the spatial clustering of summer heavy rainfall events over the Beijing metropolitan region. *J. Geophys. Res. Atmos.*, **119**, 1203–1217, https://doi.org/10.1002/2013JD020762.

——, J. A. Smith, and D. Niyogi, 2019: Urban impacts on extreme monsoon rainfall and flooding in complex terrain. *Geophys. Res. Lett.*, **46**, 5918–5927, https://doi.org/10.1029/2019GL083363.

Yu, M., and Y. Liu, 2015: The possible impact of urbanization on a heavy rainfall event in Beijing. *J. Geophys. Res. Atmos.*, **120**, 8132–8143, https://doi.org/10.1002/2015JD023336.

Zhai, P., X. Zhang, H. Wan, and X. Pan, 2005: Trends in total precipitation and frequency of daily precipitation extremes over China. *J. Climate*, **18**, 1096–1108, https://doi.org/10.1175/JCLI-3318.1.

Zhang, C. L., F. Chen, S. G. Miao, Q. C. Li, X. A. Xia, and C. Y. Xuan, 2009: Impacts of urban expansion and future green planting on summer precipitation in the Beijing metropolitan area. *J. Geophys. Res.*, **114**, D02116, https://doi.org/10.1029/2008JD010328.

Zhang, D. L., Y. Lin, P. Zhao, X. Yu, S. Wang, H. Kang, and Y. Ding, 2013: The Beijing extreme rainfall of 21 July 2012: "Right results" but for wrong reasons. *Geophys. Res. Lett.*, **40**, 1426–1431, https://doi.org/10.1002/grl.50304.

Zhang, X., L. Alexander, G. C. Hegerl, P. Jones, A. K. Tank, T. C. Peterson, B. Trewin, and F. W. Zwiers, 2011: Indices for monitoring changes in extremes based on daily temperature and precipitation data. *Wiley Interdiscip. Rev.: Climate Change*, **2**, 851–870, https://doi.org/10.1002/wcc.147.

Zhang, Y., J. A. Smith, L. Luo, Z. Wang, and M. L. Baeck, 2014: Urbanization and rainfall variability in the Beijing metropolitan region. *J. Hydrometeor.*, **15**, 2219–2235, https://doi.org/10.1175/JHM-D-13-0180.1.

Zhang, Y. C., X. Wang, L. Zhang, and J. Shu, 2017: Numerical simulation of the impacts of the sea-breeze and the urban heat island on the severe convective event in Shanghai (in Chinese). *Plateau Meteor.*, **36**, 705–717.

Zhong, S., and X. Yang, 2015: Ensemble simulations of the urban effect on a summer rainfall event in the Great Beijing Metropolitan Area. *Atmos. Res.*, **153**, 318–334, https://doi.org/10.1016/j.atmosres.2014.09.005.

——, Y. Qian, C. Zhao, R. Leung, and X. Q. Yang, 2015: A case study of urbanization impact on summer precipitation in the Greater Beijing Metropolitan Area: Urban heat island versus aerosol effects. *J. Geophys. Res. Atmos.*, **120**, 10 903–10 914, https://doi.org/10.1002/2015JD023753.

——, and Coauthors, 2017: Urbanization-induced urban heat island and aerosol effects on climate extremes in the Yangtze River Delta region of China. *Atmos. Chem. Phys.*, **17**, 5439–5457, https://doi.org/10.5194/acp-17-5439-2017.

Zhou, Z., J. A. Smith, D. B. Wright, M. L. Baeck, L. Yang, and S. Liu, 2019: Storm catalog-based analysis of rainfall heterogeneity and frequency in a complex terrain. *Water Resour. Res.*, **55**, 1871–1889, https://doi.org/10.1029/2018WR023567.